

# Model-Based Reconstruction for X-ray Diffraction Imaging

Venkatesh Sridhar<sup>a</sup>, Sherman J. Kisner<sup>a</sup>, Sondre Skatter<sup>b</sup>, and Charles A. Bouman<sup>a</sup>

<sup>a</sup>Purdue University, West Lafayette, IN, USA

<sup>b</sup>Morpho Detection Inc., Newark, CA, USA

## ABSTRACT

In this paper, we propose a novel 4D model-based iterative reconstruction (MBIR) algorithm for low-angle scatter X-ray Diffraction (XRD) that can substantially increase the SNR. Our forward model is based on a Poisson photon counting model that incorporates a spatial point-spread function, detector energy response and energy-dependent attenuation correction. Our prior model uses a Markov random field (MRF) together with a reduced spectral bases set determined using non-negative matrix factorization. We demonstrate the effectiveness of our method with real data sets.

**Keywords:** X-ray diffraction, MBIR, security

## 1. INTRODUCTION

X-ray Diffraction (XRD) Tomography is emerging as an important imaging modality for transportation security applications. Recently, baggage scanners equipped with both dual-energy Computed Tomography (CT) and XRD modalities have been deployed at airports for the inspection of carry-on luggage. XRD scanners reconstruct the voxel-wise spectral profile which is characteristic of molecular composition of the material.<sup>1-3</sup> In contrast to conventional CT imaging, this gives XRD the ability to even distinguish between materials with similar densities based on their diffraction profiles.

However, current X-ray diffraction imaging (XDi) system designs often face challenges in achieving sufficient spatial resolution and signal-to-noise ratio (SNR) due to the limited number of detected photons. One important consideration in XDi scanner design is the tradeoff between low-angle scatter detection versus wide-angle scatter detection. Wide-angle detection systems can accept scatter at high angles thereby achieving higher photon counts. However, wide-angle systems also require attenuation correction from an auxiliary X-ray transmission scan. Low-angle detectors have the important advantage that both the scattered photons and the directly transmitted photons travel along similar paths. This allows autonomous correction for attenuation, but it also reduces the photon count, making it more difficult to achieve the needed signal-to-noise ratio and resolution.

In this paper, we deal with a 3<sup>rd</sup> generation XDi scanner that implements the Multiple Inverse Fan-Beam (MIFB) geometry.<sup>2</sup> In stark comparison to 1<sup>st</sup> generation XDi topologies which scan only a single object point in time, 3<sup>rd</sup> generation systems have the capability to acquire highly-parallel measurements.<sup>2</sup> This particular advantage translates into drastic reductions in scan times of checked baggage. We propose a novel 4D model-based iterative reconstruction (MBIR) algorithm for low-angle scatter XRD that can substantially increase the SNR by fully accounting for both the forward model of the scanner and the prior model of the image. Our forward model is based on a Poisson photon counting model that utilizes a spatial point-spread function to incorporate the scanner-geometry and corrects for the energy-dependant attenuation of the X-ray spectrum along the path from source to detector. Our prior model is based on the combination of a Markov random field (MRF) spatial prior together with a reduced non-negative spectral bases set. Using these models, we compute the maximum a posteriori (MAP) estimate to render a 4D reconstruction in space and momentum spectrum. The computation of the MAP estimate is based on an iterative voxel-wise update strategy similar to that considered by *Bouman et al.*<sup>4</sup> and exploits the sparsity in photon-count measurements. We validate the performance of our reconstruction technique with actual baggage data.

---

Further author information:

E-mail<sup>a</sup>: {vsridha, kisner, bouman}@purdue.edu

E-mail<sup>b</sup>: sskatter@morphodetection.com

Anomaly Detection and Imaging with X-Rays (ADIX), edited by  
Amit Ashok, Mark A. Neifeld, Michael E. Gehm, Proc. of SPIE Vol. 9847,  
98470K · © 2016 SPIE · CCC code: 0277-786X/16/\$18 · doi: 10.1117/12.2223134

## 2. XRD FORWARD MODEL

### 2.1 Fundamentals of Coherent Scatter Detection

XDi systems utilize a range of X-ray photon energies that result in coherent scatter. In this type of X-ray interaction with matter, the incident photon does not have enough energy to ionize electrons from the atomic shell of the medium. This leads to a change in direction of the photon, but its energy remains the same.

Figure 1 illustrates the diffraction of an incident X-ray beam by a single voxel. Photons that are deflected by an angle  $\theta$  are sensed by a detector. Furthermore, let us denote the solid angle subtended by the detector as  $\Omega$ . Notice that this solid angle is dependent on both the voxel location and the detector position.

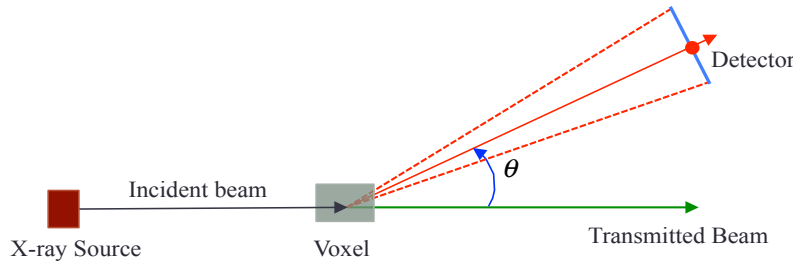


Figure 1: Illustration of X-ray diffraction and transmission. The solid red line depicts the trajectory of photons scattered at angle  $\theta$ , whereas the solid green line represents the direct path. The dotted red lines indicate the angle subtended by the detector at the voxel.

Let us assume that the voxel contains a homogenous material. Furthermore, let us assume that this material is amorphous or polycrystalline with crystal grains at random orientations that are small compared to the size of a voxel. In this general case, intensity of the scattered X-rays will generally be proportional to the quantity

$$X_g(E, \theta) = n_p \frac{d\sigma_p}{d\Omega}(E, \theta)$$

where  $n_p$  is the number density of constituent particles in the voxel (units of *particles/cm<sup>3</sup>*), and  $\frac{d\sigma_p}{d\Omega}$  is the differential cross-section of the constituent particles (units of *cm<sup>2</sup>/(sr - particle)*). Notice that the differential cross-section represents the scatter cross-section per steradian of scatter angle. Since the material composition of the object can change from voxel to voxel, the differential cross-section is a function of  $r$  as well as the energy of the photon  $E$  and the scatter angle  $\theta$ . From this definition, we see that  $X$  has units of *1/(sr - cm)*.

For the aforementioned type of material, it is commonly assumed that  $X$  is only a function of the momentum transfer, which is defined as

$$q = \frac{E}{hc} \sin\left(\frac{\theta}{2}\right). \quad (1)$$

This is a very important constraint since this means that we need must only reconstruct the quantity

$$X(q) = X_g(E, \theta),$$

where  $q$  is given as a function of  $E$  and  $\theta$ .

Let  $\lambda(E)$  be the detected photon rate for photons at a energy  $E$ . Then in general,  $\lambda(E)$  is given by

$$\lambda(E) = I_s(E) A_I(E) X(q) A_D(E) \Omega V \quad (2)$$

where  $I_s(E)$  is the source intensity at energy  $E$ ,  $A_I(E)$  is the source to voxel attenuation,  $A_D(E)$  is the voxel to detector attenuation,  $\Omega$  is the solid angle subtended by the detector, and  $V$  is the volume of the voxel. Here the photon intensity is  $I_s(E)$  has units of *photons/cm<sup>2</sup>*, and both  $A_I(E)$  and  $A_D(E)$  are unitless, so  $\lambda(E)$  has units of *photons*.

For our applications,  $\theta$  is very low, typically in the range of 0 to 50 milli-radians. This implies that the attenuation along the path from source to detector is approximately same as that experienced by the directly transmitted beam.<sup>3,5</sup> So in the low angle case this approximation can be written as

$$I_s(E) A_I(E) A_D(E) \approx f(E) , \tag{3}$$

where  $f(E)$  is the spectrum of the detected X-ray photons along the direct path. In practice,  $f(E)$  must be measured for each beam since the attenuation will be object dependent. The details on how  $f(E)$  is measured are described in the following section.

The product of the solid angle of scatter, and the voxel volume form a single constant that is not a function of energy given by

$$\beta = \Omega V .$$

In practice,  $\beta$  can be determined through a calibration procedure since it is only a function of the scanner geometry and not a function of the object being scanned.

So then the final relationship between the unknown  $X$  and the measured photon rate at energy  $E$  is given by

$$\lambda(E) = \beta f(E) X(q) \tag{4}$$

## 2.2 Data Collection and Preprocessing

Figure 2 illustrates the geometry of the XDi system. An array of sources are used to image a 2D plane through the object, which in this case, is the  $x$ - $z$  plane. Each source is collimated into a fan of X-ray pencil beams that pass through the object. However, Figure 2 merely shows what happens along one such pencil beam. A dual-energy X-ray detector measures the flux of the directly transmitted beam. An array of scatter detectors are collimated so that each detector measures the scatter at one point along the pencil beam. The collimation is performed so that the angle of scatter,  $\theta$ , is relatively small and approximately constant for all the detectors.

We will refer to the point of intersection of the pencil beam and the detector collimation as a scatter center. The scatter center represents the location of material being measured. We will index each scatter center by  $o$ , and we note that the scatter center is specified by a combination of the source  $s$  and the detector  $d$ . Equivalently, each scatter center  $o$  uniquely specifies a source-detector pair  $(s, d)$ . In addition, the object being imaged is moved through the XDi system with a belt. So each scatter center belongs to a slice through the object.

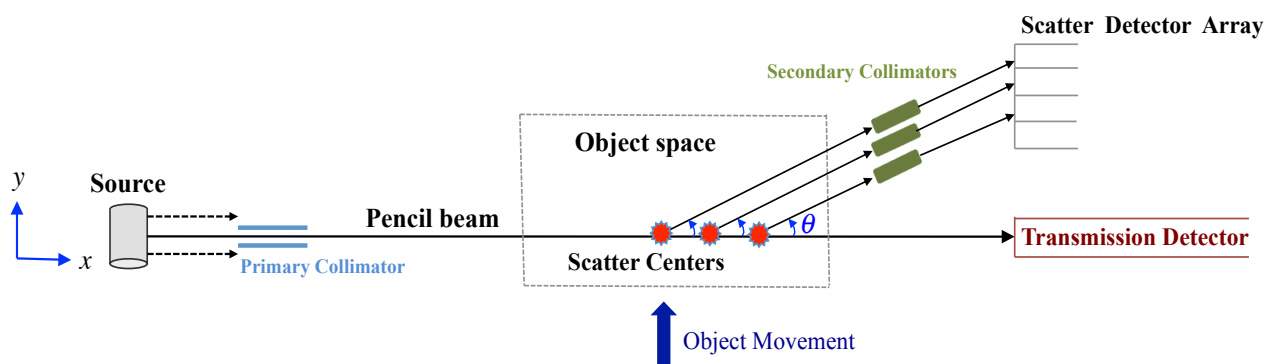


Figure 2: Schematic depicting the basic geometry of the XDi system. The measurement of scatter is localized to specific points in object-space, or scatter-centers, which are highlighted in red.

### 2.2.1 XDi List-mode Data

In order to maximize signal-to-noise, the detectors count photons and report an energy for each detected photon. This data is reported in list-mode format; so a list of photon counts with associated energy are reported for each scatter center.

More specifically, for a given scatter-center,  $o$ , the list-mode measurement data provides us three pieces of information represented by  $\{N_o, \theta_o, E_o\}$ . Here,  $N_o$  denotes the number of detected photons from the  $o$ -th scatter center, and  $E_o \in \mathbb{R}^{N_o}$  is a vector whose entry  $E_{o,i}$  represents the energy of the  $i$ -th detected photon,  $1 \leq i \leq N_o$ . The scatter-angle may deviate slightly from the nominal angle  $\bar{\theta}$  and its value for the  $o$ -th scatter center is denoted by  $\theta_o \in \mathbb{R}^+$ .

For each photon energy,  $E_{o,i}$ , we may compute an associated momentum transfer value that accounts for that the specific detector's scatter angle.

$$q_{o,i} = E_{o,i} \frac{\sin(\theta_o/2)}{hc} \quad (5)$$

The momentum transfer value is then quantized by mapping it to the closest of a set of  $N_M$  values given by  $\{\tilde{q}_m\}_{m=1}^{N_M}$ . Let  $M_{o,i}$  be this discrete quantization level. Then the photon count for the  $o$ -th scatter-center and  $m$ -th momentum bin,  $\lambda_{o,m}$ , can then be expressed as

$$\lambda_{o,m} = \sum_{i=1}^{N_o} \delta(M_{o,i} - m), \quad (6)$$

where the function  $\delta(\cdot)$  is defined as 1 when argument is 0, and 0 otherwise. So intuitively,  $\lambda_{o,m}$  is the number of photons from scatter center  $o$  that fall into momentum transfer bin  $m$ .

Assuming that  $N_M$  is sufficiently large, detected photons from a given scatter-center  $o$  that fall within the same momentum bin  $m$ , have approximately the same energy. Accounting for the detector-specific scatter angle  $\theta_o$ , we can express this discrete energy  $\tilde{E}_{o,m}$  as follows

$$\tilde{E}_{o,m} = \tilde{q}_m \frac{hc}{\sin(\theta_o/2)} \quad (7)$$

### 2.2.2 Attenuation Correction

For each scatter-center  $o$ , we estimate the momentum-spectrum of photons along the direct transmission path, represented by the vector  $I_o \in \mathbb{R}^{N_M}$ . However, note that this spectrum,  $I_o$ , accounts for the energy-dependent attenuation undergone by the detected photons. So, the  $m$ -th entry of  $I_o$  is expressed as

$$I_{o,m} = f_o(\tilde{E}_{o,m}) \quad (8)$$

where  $f_o(\cdot)$  is a function specific to the incident pencil-beam, since the attenuating medium varies for different beam-paths. The above function is common to all scatter-centers that share the same transmission path.

We derive  $f_o(\cdot)$  from the dual-energy flux measured by the transmission detector. This is accomplished through techniques similar to *Beam-Hardening* correction for dual-energy CT. A common approach is to select two basis materials with markedly different attenuation characteristics, and then decompose the medium along the direct beam path into these basis materials.<sup>6,7</sup> For this approach,  $f_o(E)$  can be determined in accordance with Beer's law, as follows

$$f_o(E) = \tilde{I}_s(E) \exp \left\{ - \sum_{j=1}^2 d_{j,o} \mu_j(E) \right\} \quad (9)$$

where  $d_{j,o}$  and  $\mu_j(E)$  represent the effective thickness and attenuation coefficient of the  $j^{\text{th}}$  basis material respectively, and  $\tilde{I}_s(E)$  denotes the source X-ray spectrum.

Estimating  $d_{j,o}$ , involves a two-step procedure. Let the pair  $\{T_{L,o}, T_{H,o}\} \in \mathbb{R}^2$  represent the dual-energy flux measured for the transmission path of the  $o$ -th scatter-center. This is dependent on the object being scanned. Let  $\{\tilde{T}_{L,o}, \tilde{T}_{H,o}\}$  represent the corresponding measurements from an air-calibration scan. First, we generate the standard dual-energy projections,  $p_{L,o}$  and  $p_{H,o}$ , defined by equation (10). Next, we apply an empirical 2<sup>nd</sup> order polynomial correction method that gives us  $d_{j,o}$  as shown in equation (11).

$$p_{L,o} = \log \left[ \frac{\tilde{T}_{L,o}}{T_{L,o}} \right] \quad \text{and} \quad p_{H,o} = \log \left[ \frac{\tilde{T}_{H,o}}{T_{H,o}} \right] \quad (10)$$

$$d_{j,o} = \gamma_{j,1} p_{L,o} + \gamma_{j,2} p_{H,o} + \gamma_{j,3} p_{L,o} p_{H,o} + \gamma_{j,4} p_{L,o}^2 + \gamma_{j,5} p_{H,o}^2, \quad j \in \{1, 2\} \quad (11)$$

The polynomial coefficients  $\gamma_{j,*}$  are obtained empirically through experiments with real objects, which are made from various compositions of the two basis materials.

### 2.2.3 Point Spread Function

The practical limitations of source and detector collimation result in scatter centers that are each spatially spread out, as opposed to narrow points in space. As shown in Figure 3, the finite aperture of the detector collimation results in the elongation of the scatter-center along the path of the incident pencil beam. Furthermore, the aperture of the source collimation, or equivalently the cross-section of the pencil beam, causes the scatter-center to also spread out along the transverse direction of the pencil beam. The overall spatial distribution of the scatter-center on the imaging plane, illustrated by the zoomed-in section of Figure 3, is modeled as a *point-spread function* (PSF). In this figure, we denote the PSF for the  $o$ -th scatter center as  $h_o(x, z)$ , where  $(x, z)$  are coordinates of any given point on the imaging plane. The PSF is only dependent on the scanner geometry, and is modeled through ray-trace simulations of the XDi system.

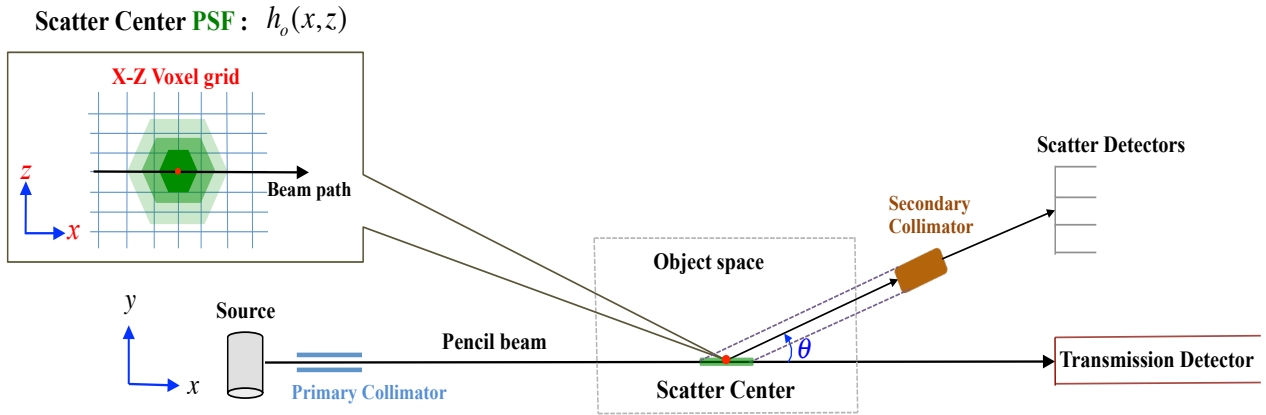


Figure 3: Schematic depicting the spatial spread of a scatter-center due to the finite aperture of the detector collimation. The zoomed in section on the left illustrates the PSF of the scatter-center on the imaging plane, where the different “rings” or contours correspond to different PSF values.

We render a sparse matrix  $H$ , whose entries  $H_{o,r}$  represent the contribution of the  $r$ -th voxel to the spatial region encompassed by the  $o$ -th scatter center.  $H_{o,r}$  is computed by finely sampling the point-spread function of the  $o$ -th scatter center,  $h_o(x, z)$ , at multiple points within the voxel  $r$ , and then taking the average of these PSF values. Finally,  $H$  is normalized such that

$$\sum_{r=1}^{N_r} H_{o,r} = 1,$$

where  $N_r$  is the total number of voxels.

### 2.3 Discretized Forward Model

Let  $X \in \mathbb{R}^{N_r \times N_M}$  represent the unknown matrix to be reconstructed, where its entries  $X_{r,m}$  denote the diffraction profile of the  $r$ -th voxel at momentum-transfer bin  $m$ . The scatter photon count received from the  $o$ -th scatter-center and  $m$ -th momentum-bin,  $\lambda_{o,m}$ , is a Poisson random variable. Along the same lines as equation (4), we can express the mean of  $\lambda_{o,m}$  as follows

$$E[\lambda_{o,m}|X] = \sum_{m'=1}^{N_M} P_{o,m,m'} \beta_o I_{o,m'} \sum_{r=1}^{N_r} H_{o,r} X_{r,m'} \quad (12)$$

where  $\beta_o$  is a geometry-dependent calibration factor that is specific to the scatter-center, and  $P_o \in \mathbb{R}^{N_M \times N_M}$ , is a matrix that accounts for the non-ideal response of the detector to various photon energies. Its entries,  $P_{o,m,m'}$ , represent the probability that a photon's detected momentum transfer falls within bin  $m$ , given that its true momentum transfer pertains to bin  $m'$ .  $P_o$  is empirically calibrated for each detector of the XDi system and is independent of the object being scanned. It is typically a lower triangular matrix, because photons impinging on a detector are most likely detected at energies roughly equal to or lower than its true energy.

### 2.3.1 Reconstruction of XRD spectrum on reduced subspace

Reconstructing the diffraction profile  $X_{r,*}$ , at every voxel  $r$ , over all  $N_M$  momentum-bins is too computationally expensive. A particular way to reduce this computational cost is to reduce the dimension of  $X$  in momentum-space. We assert that each row of  $X$  can be adequately represented by a reduced set of spectral features. The technique we apply to solve this dimensional reduction problem, coupled with a positivity constraint on  $X$ , is non-negative matrix factorization (NNMF).

We model  $X$  as a product of two matrices,  $\tilde{X}$  and  $T$ , both of which have nonnegative elements.  $\tilde{X}$  is a tall-and-thin matrix of size  $N_r \times N_p$  and  $T$  is a short-and-wide matrix of size  $N_p \times N_M$ , where  $N_p \ll N_M$ .

$$X = \tilde{X}T . \quad (13)$$

Each row of  $T$  represents a basis spectrum used to represent the momentum-spectra of  $X$ . The plots in Figure 4 are the rows of  $T$  when  $N_p = 4$ . So now, for every voxel  $r$ , instead of reconstructing the entire diffraction profile  $\{X_{r,m}\}_{m=1}^{N_M}$ , we only need to recover the  $N_p$  coefficients of the basis spectra,  $\{\tilde{X}_{r,p}\}_{p=1}^{N_p}$

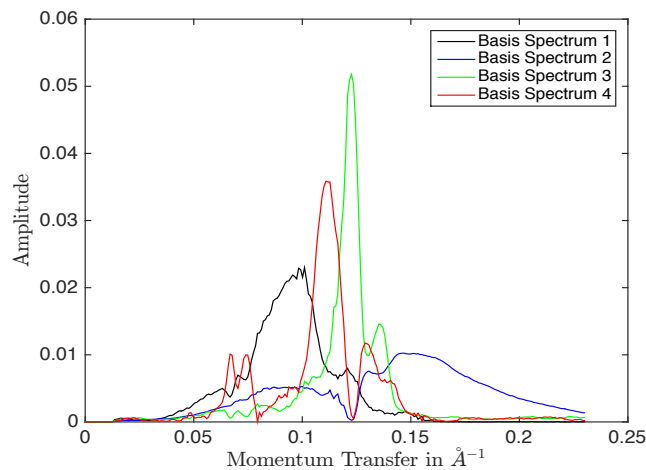


Figure 4: Basis spectra obtained through NNMF decomposition of the training data, when number of basis components,  $N_p$  is 4

Currently we use a training data set comprising the diffraction profiles of various materials of interest, acquired through an offline measurement device. Then we quickly render a  $T$  matrix by NNMF decomposition<sup>8</sup> of the training data, and normalize  $T$  such that each row sums to 1.

$$\sum_{m=1}^{N_M} T_{p,m} = 1 \quad \forall p$$

## 3. STATISTICAL MODEL AND RECONSTRUCTION APPROACH

Our framework for XDi reconstruction is based on standard *maximum a posteriori* (MAP) estimation. Let  $\lambda$  represent the matrix of photon-counts detected from each scatter-center and momentum bin. The MAP estimate

of  $X$  is formulated as

$$\hat{X} = \tilde{X}T, \quad \text{where}$$

$$\tilde{X} \leftarrow \underset{\tilde{X} \geq 0}{\operatorname{argmin}} \left\{ -\log p(\lambda|\tilde{X}) - \log p(\tilde{X}) \right\} \quad (14)$$

In the following sections we shall first discuss the likelihood and prior models,  $p(\lambda|\tilde{X})$  and  $p(\tilde{X})$  respectively, and then move on to describing an iterative optimization strategy to solve equation (14).

### 3.1 Likelihood function

The measured photon count from scatter center  $o$  and with a momentum-transfer bin  $m$  is modeled as a poisson distribution shown below

$$p(\lambda_{o,m}|\tilde{X}) = e^{-\bar{\lambda}_{o,m}} \frac{(\bar{\lambda}_{o,m})^{\lambda_{o,m}}}{\lambda_{o,m}!}, \quad (15)$$

where  $\bar{\lambda}_{o,m}$  is the mean photon count given by

$$\bar{\lambda}_{o,m} = \sum_{m'=1}^{N_M} P_{o,m,m'} \beta_o I_{o,m'} \sum_{r=1}^{N_r} \sum_{p=1}^{N_p} H_{o,r} \tilde{X}_{r,p} T_{p,m'}. \quad (16)$$

We accumulate the pre-computed coefficients that characterize the detector-response, attenuation correction, and the NNMF spectral bases in the above equation into a single parameter  $\eta$  as expressed below

$$\eta_{p,o,m} \triangleq \beta_o \sum_{m'=1}^{N_M} P_{o,m,m'} I_{o,m'} T_{p,m'} \quad (17)$$

Now, we can conveniently re-write the mean photon count as

$$\bar{\lambda}_{o,m} = \sum_{r,p} H_{o,r} \tilde{X}_{r,p} \eta_{p,o,m}. \quad (18)$$

The likelihood term assuming independence between measurements is then given by,

$$-\log p(\lambda|\tilde{X}) = \sum_{o,m} -\log p(\lambda_{o,m}|\tilde{X})$$

$$= \sum_{o,m} \left\{ \sum_{r,p} H_{o,r} \tilde{X}_{r,p} \eta_{p,o,m} - \lambda_{o,m} \log \left( \sum_{r,p} H_{o,r} \tilde{X}_{r,p} \eta_{p,o,m} \right) \right\} + c(\lambda). \quad (19)$$

The term  $c(\lambda)$  groups all additive terms that are not a function of  $X$ , which can therefore be dropped from the cost function.

### 3.2 Prior model

The prior distribution of  $\tilde{X}$  is modeled as a Markov random field (MRF) with a symmetric 26-point neighborhood system in 3-D space. The prior model of  $\tilde{X}$  incorporates a pair-wise Gibbs distribution with its general form given by

$$p(\tilde{X}) = \frac{1}{z} \prod_{p=1}^{N_p} \exp \left\{ -\frac{1}{\sigma} \sum_{(r,s) \in \mathcal{C}} b_{r,s} \rho \left( \tilde{X}_{r,p} - \tilde{X}_{s,p} \right) \right\} \quad (20)$$

where  $\mathcal{C}$  denotes the set of all pair-wise cliques in  $\tilde{X}$ , and  $\rho(\cdot)$  is the positive and symmetric *potential function*. The parameter  $\sigma$  determines the overall level of smoothing, and  $z$  is a normalizing constant. The specific prior

chosen for our application was a *Q-generalized Gaussian Markov random field*, or Q-GGMRF<sup>9</sup> prior, where shape of the potential function is controlled by the parameters  $q$  and  $c$  as expressed below

$$\rho(\Delta) = |\Delta|^p \frac{|\Delta/c|^{q-p}}{1 + |\Delta/c|^{q-p}} \quad (21)$$

The penalty levied on differences between neighboring pixel varies as  $\rho(\Delta) \approx c^{p-q}|\Delta|^q$  for very small differences where  $|\Delta| \ll c$ , and  $\rho(\Delta) \approx |\Delta|^p$  in the range where  $|\Delta| \gg c$ . This approximate piece-wise behavior of the potential function permits us to tune our prior through a suitable choice of parameters  $p$  and  $q$  to preserve both low-contrast details as well as edge characteristics. Common choice of parameters is  $p = 2$ , and  $q$  in the interval  $[1, 2]$ . Note that these values result in a convex potential function, which ultimately ensures an overall convex cost function. Selecting  $q = 1$  further simplifies the prior and its derivative, and thus expedites computation.

### 3.3 Iterative coordinate descent

To solve the multi-variable optimization problem posed by equation (14), we use the iterative coordinate descent (ICD) strategy which minimizes the cost function  $g(\tilde{X})$  through a series of successive 1D minimizations.<sup>4,10</sup> Substituting expressions for the log likelihood and log prior in equation (14), the global cost function is

$$g(\tilde{X}) = \sum_{o,m} \left\{ \sum_{r,p} H_{o,r} \tilde{X}_{r,p} \eta_{p,o,m} - \lambda_{o,m} \log \left( \sum_{r,p} H_{o,r} \tilde{X}_{r,p} \eta_{p,o,m} \right) \right\} + \frac{1}{\sigma} \sum_p \sum_{(r,s) \in \mathcal{C}} b_{r,s} \rho(\tilde{X}_{r,p} - \tilde{X}_{s,p}) \quad (22)$$

Note that since the above cost function is convex, our optimization algorithm ultimately converges to the global minimum. Here each ICD update minimizes the cost function with respect to a single optimization variable keeping all the other  $N_r N_p - 1$  variables fixed. The update for the voxel  $s$  and spectral feature  $q$  is given by

$$\tilde{X}_{s,q} \leftarrow \underset{u \geq 0}{\operatorname{argmin}} g_l(u) \quad , \text{ where} \quad (23)$$

$$g_l(u) = \sum_{o,m} \left\{ u H_{o,s} \eta_{q,o,m} - \lambda_{o,m} \log \left[ (u - \tilde{X}_{s,q}) H_{o,s} \eta_{q,o,m} + \sum_{r,p} H_{o,r} \tilde{X}_{r,p} \eta_{p,o,m} \right] \right\} + \frac{1}{\sigma} \sum_{r \in \partial s} b_{s,r} \rho(u - \tilde{X}_{r,q}) \quad (24)$$

and  $\partial s$  denotes the neighborhood of voxel  $s$  and  $g_l(u)$  is the localized cost function.

The solution to equation (23) does not have a closed form expression. However, because  $g_l(\cdot)$  is convex, the solution can be obtained by finding the root of the local cost function's derivative  $g'_l(u)$ . By exploiting the sparse nature of both the PSF matrix  $H$  and measurements  $\lambda$ , the computation of  $g'_l(u)$  can be accelerated.

## 4. RESULTS AND DISCUSSION

To validate our forward model and ICD optimization algorithm, we perform reconstructions on XRD measurements acquired from actual baggage. Further we investigate the effect of various parameters such as the voxel resolution, level of regularization contributed by the prior, and the dimensionality of the reduced spectral subspace,  $N_p$ , on the quality of reconstruction.

A key benefit of introducing the point spread function to the reconstruction is that it allows flexibility in the definition of the voxel grid in object space. More, specifically we can reconstruct at any spatial resolution we choose. However, beyond some spatial sampling rate, we will no longer recover any additional spatial resolution.

Figure 5 depicts various reconstructions of a test bag containing two bottles filled to capacity with two different liquids. The conventional X-ray transmission image of the bag taken prior to the scan is shown in (a). The two liquids in this bag have similar densities. Their scatter-strengths, which is the sum of the diffraction spectra over all momentum-bins, differ by less than 15%.

Back-projection of the photon-count measurements onto the voxel grid using a high resolution PSF matrix  $H$  is shown in (b). The reconstructed images (c) to (f) represent the scatter-strength, which in this case is the

sum of  $\tilde{X}$  over all  $N_p$  basis components, because each basis spectrum sums to 1. First, we investigate if we can extract finer spatial information from the XDi bag scans by decreasing the voxel size. Results (c) and (d) pertain to reconstructions performed at the standard voxel size of the scanner. We then tried doubling resolution in each spatial dimension and re-defined the PSF matrix accordingly. We were able to achieve enhanced image quality as illustrated by the resulting high-resolution reconstructions in (d) and (e). Next, we examine the effect of the prior on image quality. A comparison of results (d) vs (f), and (c) vs (e) demonstrates that a higher level of regularization results in greater smoothness and removal of high-contrast artifacts.

Figure 6 shows the reconstructed momentum spectrum of the two liquids in the scanned bag. The spectra are averaged over the volume of each bottle and displayed for reconstructions with different values of  $N_p$ . In general, most liquids have relatively smooth diffraction profiles, rather than a rugged profile with several sharp peaks that solid crystals and powders usually exhibit. Typically, accounting for a higher number of basis spectra should lead to major improvements in the reconstructed spectral profile and cause it to converge towards the true spectrum. In our current example, the spectral reconstructions do not vastly vary between using four and six basis components, because the predominant spectral features in the actual data resemble the 2<sup>nd</sup> basis spectrum in Figure 4.

## 5. CONCLUSION

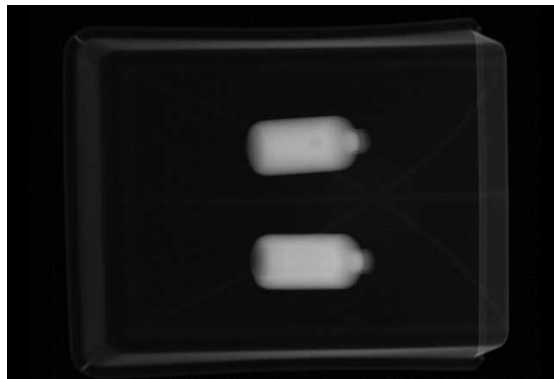
In this paper, we have presented a 4-D model-based iterative reconstruction (MBIR) method for a low-angle detection XDi scanner. We have proposed a novel forward model that includes a system-dependent spatial point-spread function, corrects for the energy-dependent X-ray attenuation, and also captures the non-ideal energy-response of the detectors. To reduce computational cost, we represented the unknown spectra with a reduced spectral bases. Reconstructions with real bag data show that it is possible to achieve sufficient spatial resolution despite very low photon counts.

## ACKNOWLEDGMENTS

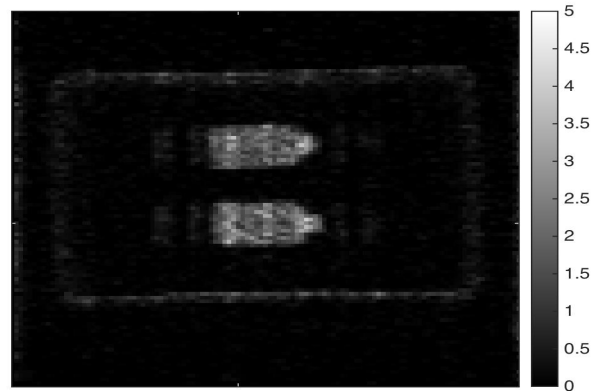
We acknowledge support from the U.S. Department of Homeland Security Science and Technology Directorate under Award Number HSHQDC-11-C-00014, and Morpho Detection Inc., Newark, CA. We also thank Geoffrey Harding and Gabriel Zienert from Morpho Detection GmbH, Germany, for their comprehensive documentation of the XDi system geometry.

## REFERENCES

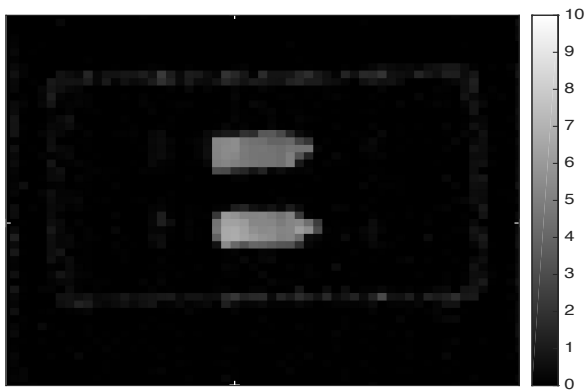
- [1] van Stevendaal, U., Schlomka, J. P., Harding, A., and Grass, M., "A reconstruction algorithm for coherent scatter computed tomography based on filtered back-projection," *Medical Physics* **30**, 2465–2474 (September 2003).
- [2] Harding, G., Strecker, H., Kosciuszka, D., and Gordon, J., "Detector considerations relevant to x-ray diffraction imaging for security screening applications," in [*Proc. SPIE, Optics and Photonics in Global Homeland Security and Biometric Technology for Human Identification*], **7306**(19), 1–11 (2009).
- [3] Harding, G., Kosanetzky, J., and Neitzel, U., "X-ray diffraction computed tomography," *Medical Physics* **14**, 515–525 (July 1987).
- [4] Bouman, C. A. and Sauer, K., "A unified approach to statistical tomography using coordinate descent optimization," *IEEE Trans. on Image Processing* **5**, 480–492 (March 1996).
- [5] Chen, K. and Castanon, D. A., "A regularized iterative reconstruction algorithm for X-Ray Diffraction Tomography," in [*Proc. SPIE, Next-Generation Spectroscopic Technologies*], **8374**, D1–D11 (2012).
- [6] Jin, P., Bouman, C. A., and Sauer, K. D., "A model-based image reconstruction algorithm with simultaneous beam hardening correction for X-Ray CT," *IEEE Transactions on Computational Imaging* **1**, 200–216 (September 2015).
- [7] Herman, G. T., "Correction for beam hardening in computed tomography," *Physics in Medicine and Biology* **24**(1), 81–106 (1979).



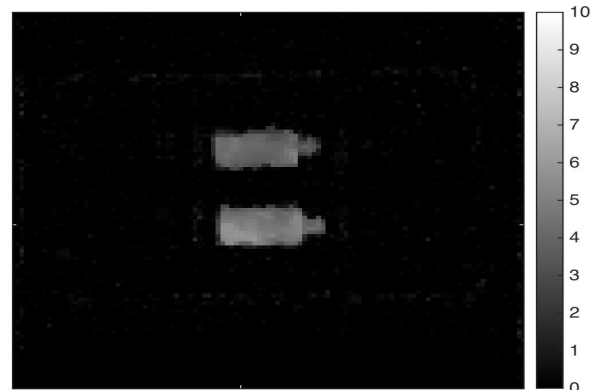
(a) Transmission prescan image



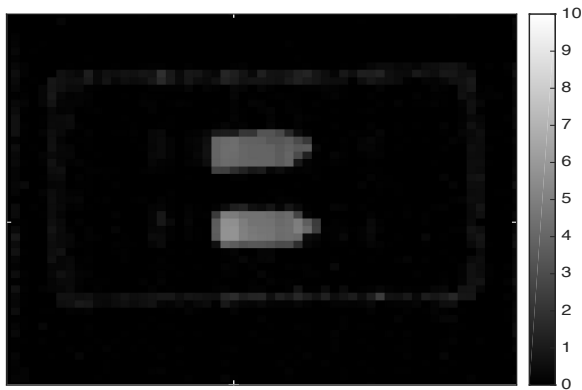
(b) Back-Projection with PSF, high resolution



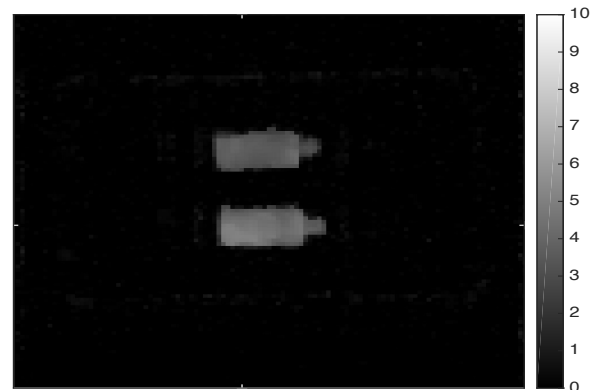
(c) Reconstructed, low resolution,  $\sigma = 1.2$



(d) Reconstructed, high resolution,  $\sigma = 1.2$



(e) Reconstructed, low resolution,  $\sigma = 0.6$



(f) Reconstructed, high resolution,  $\sigma = 0.6$

Figure 5: Model-based scatter strength reconstructions of an actual bag, with its prescan image depicted in (a). All slices shown are coronal, i.e. looking down on the scanner tunnel. In (d) and (f), the voxel size is halved in all 3-dimensions. The number of basis spectra  $N_p$  was chosen to be 4.

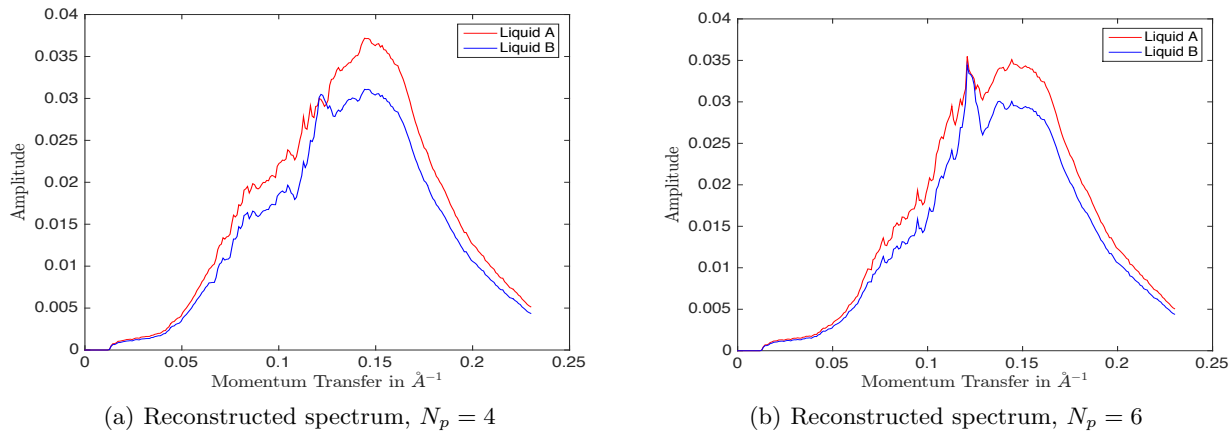


Figure 6: The diffraction profiles of two liquids A and B, contained within the bottles of the scanned bag. The reconstruction parameters are same as that used in obtaining the high-resolution result in figure 5(f).

- [8] Berry, M. W., Browne, M., Langville, A. N., Pauca, V. P., and Plemmons, R. J., "Algorithms and applications for approximate nonnegative matrix factorization," *Computational Statistics & Data Analysis* **52**(1), 155–173 (2007).
- [9] Thibault, J.-B., Sauer, K., Bouman, C., and Hsieh, J., "A three-dimensional statistical approach to improved image quality for multi-slice helical CT," *Medical Physics* **34**(11), 4526–4544 (2007).
- [10] Sauer, K. and Bouman, C., "A local update strategy for iterative reconstruction from projections," *IEEE Trans. on Signal Processing* **41**, 534–548 (February 1993).